

The Kormendy relation of cluster galaxies in PPS regions

A.L.B. Ribeiro¹, [★] P.A.A. Lopes², D.F. Morell³, C.C. Dantas⁴, M.H.S. Fonseca²,
B.G. Amarante¹, F.R. Morais-Neto¹

¹Laboratório de Astrofísica Teórica e Observacional, Universidade Estadual de Santa Cruz, Ilhéus, BA 454650-000, Brazil

²Observatório do Valongo, Universidade Federal do Rio de Janeiro, RJ 20080-090, Brazil

³Instituto de Astronomía, Universidad Nacional Autónoma de México, Apartado Postal 70-264, Ciudad de México, D.F., México

⁴Instituto Nacional de Pesquisas Espaciais/MCTI, SP 12227-900, Brazil

Accepted XXX. Received YYY; in original form ZZZ

ABSTRACT

We study a sample of 936 early-type galaxies located in 48 low- z regular galaxy clusters with $M_{200} \geq 10^{14} M_{\odot}$ at $z < 0.1$. We examine variations in the Kormendy relation (KR) according to their location in the projected phase space (PPS) of the clusters. We have used a combination of Bayesian statistical methods to identify possible differences between the fitted relations. Our results indicate that the overall KR is better fitted when we take into account the information about PPS regions. We also find that objects with time since infall ≥ 6.5 Gyr have a significant statistical difference of the KR coefficients relative to objects that are more recent in the cluster environment. We show that giant central ellipticals are responsible for tilting the KR relation towards smaller slopes. These galaxies present a late growth probably due to cumulative preprocessing during infall, plus cannibalism and accretion of smaller stripped objects near the center of the clusters.

Key words: galaxies: evolution; galaxies: elliptical and lenticular, cD; galaxies: clusters

1 INTRODUCTION

The Kormendy relation (KR) is a relation between the effective radius R_e of Early-Type Galaxies (ETGs) and the surface brightness μ_e at that radius (Kormendy 1977). It is a projection of the Fundamental Plane of galaxies, a three-dimensional parameter space correlating, in addition to R_e and μ_e , the velocity dispersion σ of galaxies (Dressler et al. 1987; Djorgovski & Davis 1987; Bender et al. 1992). The KR is a scaling relation indicating that more luminous objects are larger and have a lower characteristic surface brightness.

ETGs encompass objects that normally ceased their star formation, have red colors, small amounts of cold gas and dust, and which correspond morphologically to ellipticals and lenticulars (e.g. Kauffmann et al. 2004; Blanton & Moustakas 2009). Some studies indicate that the formation of massive ETGs has occurred in two phases (e.g. Oser et al. 2010). At an early stage, the gas collapses into dark matter halos and forms stars intensely for a short time interval (e.g. Thomas et al. 2005; Peng et al. 2010; Conroy et al. 2015). The second phase involves mass accumulation through a series of mergers (e.g. Naab et al. 2009; Feldmann et al. 2011; Johansson et al. 2012; Huang et al. 2016) that enrich galaxies with stars set *ex-situ*, thereby increasing their size and stellar mass continuously (e.g. Trujillo et al. 2007; Van Dokkum et al. 2010).

The structural analysis of ETGs through various scaling relations can be used to probe the evolutionary state of galaxies and constrain galaxy formation models and the assembly history of ETGs (e.g.

Tortorelli et al. 2018; Genel et al. 2018; Kuchner et al. 2022). In particular, the KR can be used to derive luminosity and size evolution of ETGs, but it requires homogeneous and complete data samples for clusters at different redshifts, wavelengths, magnitude range, taking into account differences between fitting methods, besides measurement and systematic errors (e.g. Ziegler et al. 1999; La Barbera et al. 2003; Kuchner et al. 2017; Tortorelli et al. 2018). All of this makes it difficult to compare results from different studies.

In this work, we address this problem by studying a homogenous sample of ETGs selected from regular galaxy clusters (Ribeiro et al. 2023). Our aim is to study the KR in subsamples defined in the projected phase space (PPS) of the clusters. The correlation between these regions and the time since infall in clusters is used to probe environmental and evolutionary effects on the coefficients of the KR. A brief description of our data is presented in Section 2. Our analysis and results are presented in Section 3. We summarize and list some conclusions in Section 5.

2 DATA

Our sample is selected from the extended version of FoF group catalog originally identified by Berlind et al. (2006) and contains 5352 groups with $N > 5$ and $0.03 \leq z \leq 0.11$, consisting of galaxies with absolute magnitudes $M_r \leq -20.5$, and stellar masses in the range $10.4 < \log(M_*/M_{\odot}) < 11.9$,¹ with median $\sim 10^{11} M_{\odot}$. The list

[★] E-mail: albr@uesc.br

¹ We use the notation “log x ” as indicating the decimal logarithm of x .

of members for each group was defined using the “shifting gapper” technique (Fadda et al. 1996; Lopes et al. 2009), extending to ~ 4 Mpc around the group centers defined by La Barbera et al. (2010). The groups were then subject to the virial analysis, analogous to that described in Girardi et al. (1998); Popesso et al. (2005, 2007); Biviano et al. (2006); Lopes et al. (2009). This procedure yields estimates of velocity dispersion (σ_v), radii (R_{500} , R_{200}) and masses (M_{500} , M_{200}) for most of the groups from the FoF sample. Our final sample contains 107 massive clusters, with at least 20 galaxies within R_{200} , implying systems with $M_{200} \gtrsim 10^{14} M_\odot$ extending to $2R_{200}$. We reduce this sample even further, demanding that the systems do not have substructures according to the DS test (Dressler & Shectman 1988); and with Gaussian velocity distribution, according to the HD metric (see Ribeiro et al. 2013; de Carvalho et al. 2017). We also added morphology from the Domínguez Sánchez et al. (2018) catalog, and the Sérsic indices n in the r -band from the catalog of Simard et al. (2011). Our final sample has 936 ETGs as objects with morphological parameter $T < 0$, probability of being a bulge-dominated object $P_{bulge} > 0.5$, and Sérsic index $n > 2.5$, located in 48 regular clusters. For more details, see Ribeiro et al. (2023).

3 ANALYSIS

We study our stacked sample of cluster ETGs according to their loci in the PPS, which is built by normalizing the projected clustercentric distances and velocities by the virial radius, R_{200} , and velocity dispersion, σ_v , respectively. To explore the PPS, we divide cluster galaxies into four subsamples, following the classification introduced by Rhee et al. (2017), see also Ribeiro et al. (2023). It is important to consider possible differences between our definitions and those used by Rhee et al. (2017), specifically our use of R_{200} and their use of R_{vir} , which are generally not equivalent (see Rhee et al. 2020). We derive a first estimate of the virial mass from equation 5 of Girardi et al. (1998). After applying the surface pressure term correction to the mass estimate, we assume a NFW profile to obtain an estimate of M_{200} . This is found after the interpolation (most cases) or extrapolation of the virial mass M_V from R_A to R_{200} (R_A is the radial offset of the most distant cluster member). Then, we use the definition of M_{200} and a final estimate of R_{200} is derived. Further details can be found in Lopes et al. (2009). With this definition, $R_{vir} \approx 1.36 R_{200}$ in the Λ CDM cosmology (see Gill et al. 2005; Reiprich et al. 2013), which may introduce a bias to our results. In order to assess for any systematic effects, we performed a series of tests and found that the present analysis remains robust and is not significantly impacted by this difference in the radial normalization of the clusters. Consequently, we have chosen to maintain PPS normalization using R_{200} .

In Figure 1 we see the distribution of ETG galaxies in the PPS regions of Rhee et al. (2017), following the approximation of Song et al. (2018). All the ancient (171 objects), intermediate (157 objects), recent (307 objects), and first infallers (301 objects) are shown in this figure. A schematic curve illustrates the expected trajectory of a galaxy through the PPS, and therefore indicates that an object in the “ancient” region requires a long time to delve into the potential of the cluster (typically more than 6.5 Gyr - see e.g. Rhee et al. 2017).

3.1 The Kormendy relation

The Kormendy relation (KR) defines an observational correlation between effective radius and surface brightness of ETGs, usually expressed as $\mu_e = \alpha + \beta \log R_e$ (Kormendy 1977). This relation provides information on the distribution of the light profiles and the

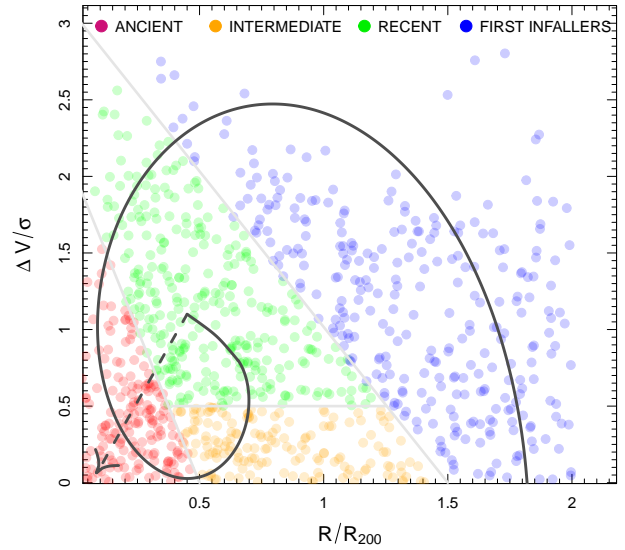


Figure 1. Distributions of ETGs in different PPS regions. Ancient objects are in red, intermediate in orange, recent in green, and the first infallers are in blue. A schematic curve illustrates the expected trajectory of a galaxy through the PPS.

sizes of ETGs, thus it can be used to study their size-evolution as a function of the environment, in particular the PPS regions.

The effective radii are calculated by

$$R_e = a_{\text{deV}} \sqrt{b/a} \quad (1)$$

where a_{deV} and b/a are the semimajor axis length and the axis ratio from the de Vaucouleurs fit, respectively. We only use ETGs with $b/a > 0.3$ to avoid edge-on objects, and $100 < \sigma < 420 \text{ km s}^{-1}$ (see Ribeiro et al. 2023). These restrictions on σ and b/a reduce the sample to 912 galaxies. The parameters a_{deV} and b/a in r -band are taken from the catalogs PhotObjAll and SpecObjAll of DR15 (Aguado et al. 2019).

We transformed the surface brightness μ_e at R_e to $\langle \mu_e \rangle$ using the relation

$$\langle \mu \rangle_e = m_r + 5 \log R_e + 2.5 \log 2\pi, \quad (2)$$

recalling that we now have

$$\langle \mu \rangle_e = \alpha' + \beta \log R_e, \quad \text{with } \alpha' = \alpha - 1.4 \quad (3)$$

(e.g. Graham & Colless 1997; Longhetti et al. 2007). This is assumed for the rest of the analysis, but for simplicity we keep the nomenclature α .

3.2 The KR fitting - all data

We begin our analysis by asking whether classifying the data according to PPS regions influences the result of the linear regression. We first ran the robust linear regression with M-estimator for all ETGs, regardless of the PPS region. Then, we ran the regression once more, now considering the region as a categorical predictor.

$$\begin{cases} \langle \mu \rangle_e &= \alpha + \beta \log R_e \\ \langle \mu \rangle_e &= (\alpha + \beta \log R_e) \cdot \text{region} \end{cases} \quad (4)$$

Hence, “region” is a categorical variable including the interaction

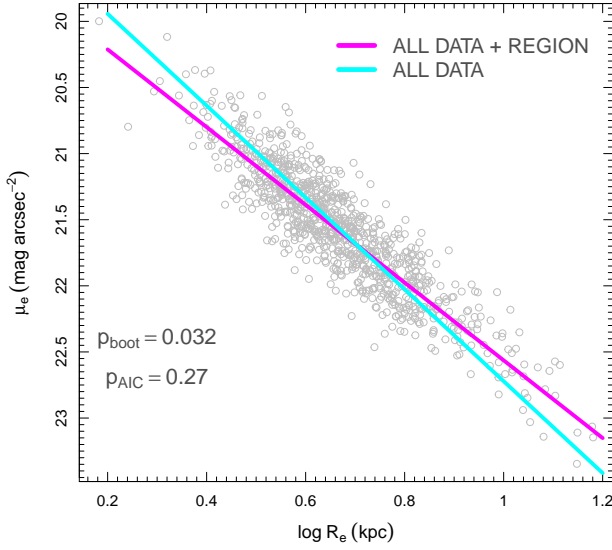


Figure 2. Linear regressions including (magenta) or not (cyan) the region as an interaction term on the slope.

effect of PPS loci on the coefficients of the KR relation. The results are presented in Figure 2. We note that both the slopes and intercepts are slightly different between the models: $\alpha = 19.62 \pm 0.19$ and $\beta = 2.94 \pm 0.26$ (including the PPS regions); or $\alpha = 19.24 \pm 0.11$ and $\beta = 3.47 \pm 0.15$ (not including the PPS regions). We compared the models using the Akaike Information Criterion (AIC) difference for the respective likelihoods, finding $\Delta_{\text{AIC}} = 2.59$, which provides strong support in favor of the model with influence from the PPS regions. We can assign a probability to the alternative model, without influence, as

$$p_{\text{AIC}} = \exp\left(\frac{-\Delta_{\text{AIC}}}{2}\right), \quad (5)$$

which provides a relative probability that the alternative model minimizes the AIC. We find $p_{\text{AIC}} = 0.27$, which is low but not entirely convincing. Then we resample the data 1000 times and check how many times the alternative model minimizes the AIC. This procedure results in only 3.2% probability (p_{boot}) favoring the alternative model, which gives us confidence about the influence of the PPS regions to explain the KR.

3.3 The KR fitting in PPS regions

The KR fitting is sensitive to sample selection effects as well as to fitting procedures (e.g. Ziegler et al. 1999; La Barbera et al. 2003; Tortorelli et al. 2018). In particular, ETGs in clusters define the KR with a high intrinsic dispersion, probably due to measurement and systematic errors. (e.g. La Barbera et al. 2003; Nigoche-Netro et al. 2008) Then, we chose to perform a Bayesian linear regression to recover the whole range of inferential solutions, i.e. the posterior distributions of the KR coefficients, rather than a point estimate and a confidence interval as in classical regression. The model is defined as

$$\langle \mu \rangle_e \sim \mathcal{N}(\alpha + \beta \log R_e, \sigma^2). \quad (6)$$

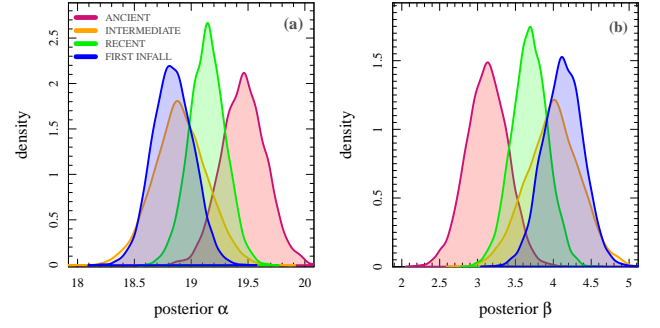


Figure 3. Posterior regression parameters from the Bayesian fits. Ancients objects are in red, intermediate in orange, recent in green, and the first infallers are in blue.

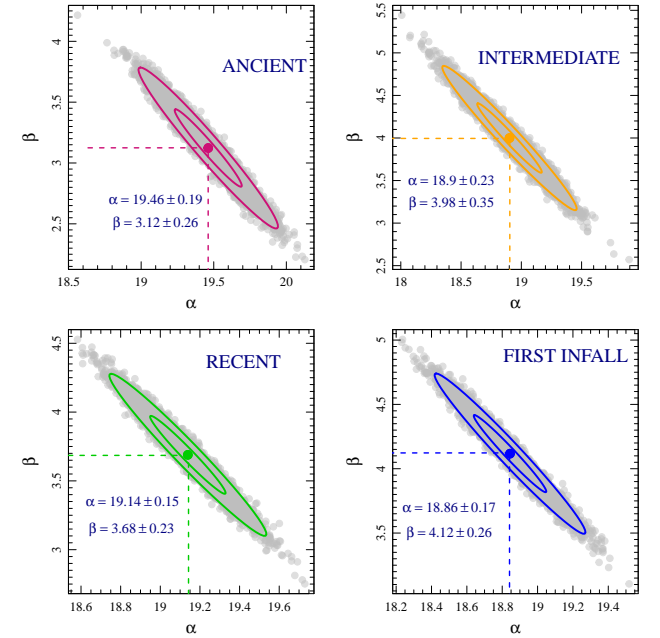


Figure 4. Confidence ellipses of parameters from the Bayesian linear fit at levels 50% and 95%. Ellipses for ancients objects are in red, intermediate in orange, recent in green, and the first infallers are in blue.

That is, we assign to the parameters a bivariate normal with noise being independent, normally distributed random variables, $\epsilon_i \sim \mathcal{N}(0, \sigma^2)$. The normal priors are taken from the best fit we found in Section 3.2. From the normal-normal conjugacy we know that the posterior distributions for each regression is also normal distributed (e.g. Lock et al. 2020). The posteriors are presented in Figure 3, with the corresponding bivariate distributions in Figure 4 for 5000 Markov-Chain-Monte-Carlo (MCMC) samples. The differences observed in these figures need to be tested and quantified. For this purpose, we use Bayesian posterior distributions for hypothesis testing. Methods include the Bayes factor two sample t-test (e.g. Morey & Rouder 2011), the Bayesian p-value based on the density at the Maximum A Posteriori (MAP) (e.g. Mills 2018), the region of practical equivalence (ROPE) (e.g. Kelter 2022) and the probability of direction (PD) (e.g. Makowski et al. 2019). These methods are briefly described in Appendix A. In all cases the quantity to be tested is the difference of slopes and intercepts (δ) between two posterior distributions from the Bayesian regressions with respect to different PPS regions. We define the PPS regions as 1 - ancient; 2 - inter-

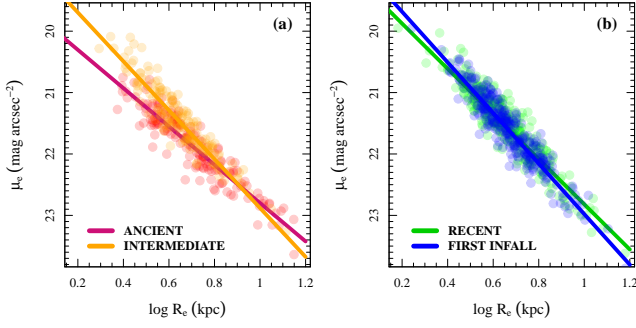


Figure 5. Linear regressions including for all subsamples. Colors indicate (a) Ancient (red) and Intermediate (orange); (b) Recent (green) and First Infall (blue).

Table 1. Results of the Bayesian tests for intercepts α . Significant differences are highlighted in red.

DATA	BF	MAP	ROPE	PD
δ_{12}	0.041	0.033	0.014	0.027
δ_{13}	0.038	0.045	0.034	0.018
δ_{14}	0.044	0.047	0.048	0.021
δ_{23}	0.032	0.238	0.189	0.037
δ_{24}	0.278	0.333	0.534	0.199
δ_{34}	0.048	0.233	0.047	0.036

Table 2. Results of the Bayesian tests for slopes β . Significant differences are highlighted in red.

DATA	BF	MAP	ROPE	PD
δ_{12}	0.001	0.034	0.034	0.038
δ_{13}	0.022	0.289	0.023	0.047
δ_{14}	0.019	0.044	0.034	0.028
δ_{23}	0.048	0.358	0.037	0.043
δ_{24}	0.342	0.457	0.212	0.327
δ_{34}	0.044	0.388	0.039	0.047

diates; 3 - recent; and 4 - first infall. Accordingly, the differences of the posteriors are written as δ_{ij} , where i and j refer to two different regions of the PPS.

Our results are summarized in Tables 1 and 2, where we notice an almost complete agreement between the methods. Red cells indicate cases in which the tests reject the null hypothesis that slopes and/or intercepts are equivalent. It is clear from the p-values in these tables that the most conservative test is the MAP-based one, and that all tests agree that there is no significant difference between galaxies taken from the intermediate and first infall regions. This result is a little surprising since, considering the time since infall, these are not regions in direct sequence. In fact, the steepest Kormendy relations are precisely those of intermediate and first infall galaxies. Objects in the recent region are in the middle, while the lowest slope comes from ancient galaxies, as we can also see in Figure 5. Being conservative, we assume the results of the MAP test and interpret that the strongest and most relevant difference between the regressions is the one that distinguishes ancient objects from the other subsamples. BCGs could be affecting this result (Ribeiro et al. 2023), but removing them does not change the result [$(\alpha_{\text{BCG}} = 19.25 \pm 0.19)$; $(\beta_{\text{BCG}} = 2.95 \pm 0.27)$]. Likewise, removing the lenticulars we found no significant difference in the fittings at the 95% confidence level. This suggests an environmental-evolutionary explanation to understand the particular behavior of the KR for ancient galaxies.

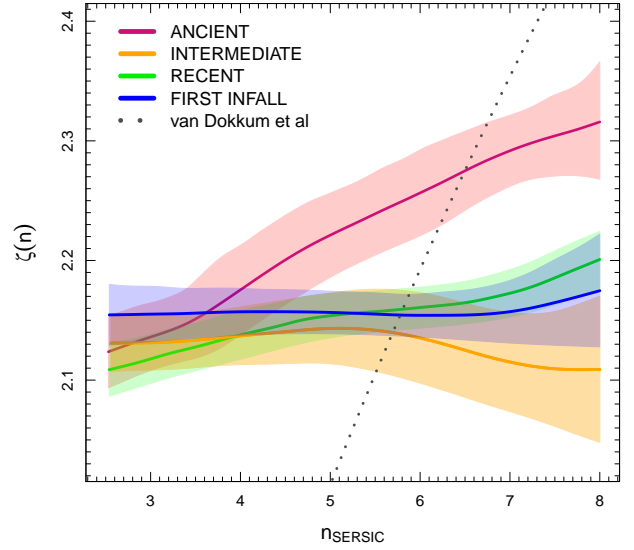


Figure 6. Growth of R_e with stellar mass for all sub-samples. Colors indicate: Ancient (red); Intermediate (orange); Recent (green); and First Infall (blue). The gray dotted line corresponds to the expected relation of $\zeta(n)$, while shaded areas show the confidence intervals calculated from 1000 bootstrap realizations.

3.4 Mass-radius relation

One can study changes in the KR by considering the evolution of luminosity at a certain R_e (e.g. La Barbera et al. 2003), or through the relative growth of the size of objects in relation to their stellar mass (e.g. Van Dokkum et al. 2010; van der Wel et al. 2014). In this work, we explore this second approach. Galaxy size is a property that is found to significantly vary with galaxy mass, star-formation activity, and redshift (e.g. Shen et al. 2003; Genel et al. 2018). In this context, the mass-radius relationship is of fundamental importance for probing changes in the KR. Usually, it is assumed to be a power law (e.g. Shen et al. 2003; van der Wel et al. 2014), describing the growth of R_e with the stellar (or total) mass. According to Van Dokkum et al. (2010) the variation of the effective radius R_e with M_* is given by

$$\frac{d \log(R_e)}{d \log(M_*)} \approx 3.56 \log(n + 3.09) - 1.22. \quad (7)$$

We call this variation $\zeta(n)$, and we used it to investigate possible differences between our subsamples. The idea to be tested is whether the time since infall promotes different behaviors for the ETG in clusters. Using the interpolation of lagged and iterated differences of R_e and M_* we compute the smoothed behaviour of $\zeta(n)$, presented in Figure 6. In this figure, we highlight three points: (i) ancient objects present a significant growth in size with respect the stellar mass; (ii) all the remaining objects present a nearly constant growth, a significant deviation from the power law expectation; and (iii) the Van Dokkum et al. (2010) growth line is steeper than the ancient behaviour.

This result clearly indicates a stronger environmental effect on galaxies longer within clusters. According to Hilz et al. (2013), a key factor to understand the inside-out growth scenario is the mass-ratio of merging galaxies, such that for minor mergers, the sizes grow significantly faster and the profile shapes change more rapidly. Ribeiro et al. (2023) found a significant change of both size and

shape (given by the Sérsic index) for ancient satellites, suggesting the relevance of possible mergers.

It is important to note that major mergers are supposed not to occur once galaxies have established themselves in the ancient region, an environment unsuitable for such mergings. The process takes place over time across the other regions, possibly through preprocessing in infall groups (see e.g. Lopes et al. 2024). On the other hand, it is known that central galaxies gradually swallows their smaller companions as dynamical friction brings them to the cluster center, growing both in size and mass, while losing velocity dispersion (e.g. Goto 2005). The growth of R_e with the stellar mass for ancient ETGs seen in Figure 6 aligns with the likelihood of minor mergers and cannibalism, as supported by the aforementioned dynamical friction in the central regions of clusters. In fact, at least 30% of the mass accreted by central galaxies since $z \approx 1$ is expected to come from mergers and accretion from stripped satellites (e.g. Laporte et al. 2013; Nipoti et al. 2018; Ragone-Figueroa et al. 2018; Chu et al. 2021). This sets a lookback time of ≈ 7.6 Gyr, which is close to the lower limit of the time since the infall for the ancient objects (Rhee et al. 2017).

4 DISCUSSION

The Kormendy relation links the effective surface brightness of ETGs to their effective radius. Our findings indicate a relevant role for the environment in establishing this relationship. Basically, we see that objects in the ancient region of the clusters present a tilt towards smaller slopes of the linear fit. To better understand this result, we split the sample of ancient ETGs into BCGs, satellites with low mass ($M_* < 10^{11} M_\odot$ – LM ANC SAT), and satellites with high mass ($M_* \geq 10^{11} M_\odot$ – HM ANC SAT). Ribeiro et al. (2023) verified a change in the behavior of the structural properties of galaxies close to this value, which is also approximately the median stellar mass of the entire sample. The subsample of BCGs is composed of the 48 most luminous ancient cluster ETGs (each taken from a cluster) having $M_r < -21.4$ and $M_* \geq 10^{11} M_\odot$ (see Ribeiro et al. 2023). The LM and HM ancient satellites samples contain 56 and 67 objects, respectively. We also consider a sample of isolated early-type galaxies taken from the list of 1-member groups of the catalog of Yang et al. (2007). This field sample, composed of 6670 objects, is defined with the same criteria (except membership) used to select the cluster ETGs (see also Ribeiro et al. 2023).

We compared the linear coefficients of the KR relation for each subsample, following the procedure described in Section 3.3. The confidence ellipses of the parameters from the Bayesian linear fit are presented in Figure 7, where the bivariate distributions correspond to 5000 Markov-Chain-Monte-Carlo (MCMC) samples. Using the methods described in Section 3.3 and Appendix A, we find no significant difference between the intercepts of the subsamples. The result of the slope comparison is presented in Table 3. Numbers 1 to 4 indicate the datasets LM SAT, HM SAT, BCGs, and FIELD galaxies, respectively.

The strongest result is the statistical evidence of a smaller slope for HM ancient satellites with respect to the other subsamples, see Figure 7. For HM ANC SAT, $\sim 90\%$ of objects have $T < -2$, so they are dominated by massive ellipticals. Our result indicates that this population is likely responsible for tilting the KR relation towards smaller slopes. On the other hand, the comparison for BCGs does not suggest a significant difference in relation to the other subsamples, except the HM ANC SAT. This result does not agree with Samir et al. (2020) who find smaller slopes for BCGs in relation to the field.

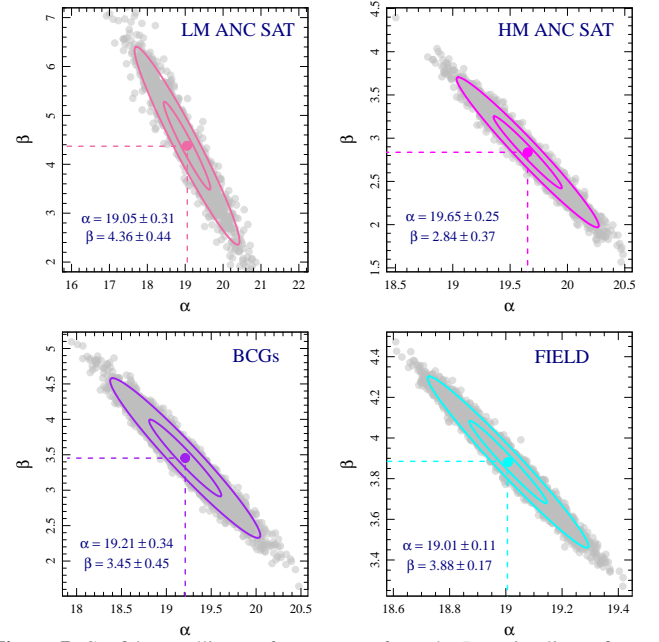


Figure 7. Confidence ellipses of parameters from the Bayesian linear fit at levels 50% and 95%. Colors indicate Low Mass Ancient Satellites (pink), High Mass Ancient Satellites (magenta), BCGs (purple), and Field galaxies (cyan).

Table 3. Results of the Bayesian tests for slopes β of subsamples of LM SAT, HM SAT, BCGs, and FIELD galaxies.

DATA	BF	MAP	ROPE	PD
δ_{12}	0.001	0.003	0.004	0.005
δ_{13}	0.047	0.115	0.043	0.236
δ_{14}	0.298	0.322	0.145	0.379
δ_{23}	0.009	0.188	0.027	0.039
δ_{24}	0.008	0.016	0.031	0.018
δ_{34}	0.126	0.333	0.284	0.227

This disagreement may be related to differences in the definition of BCGs, as well as to uncertainties in the brightness profiles of these objects, which are difficult to map due to the presence of many other galaxies close to them. In fact, for mergers occurring at late times, BCGs mainly accrete mass into their extended outskirts, beyond the observational photometry apertures (e.g. Inagaki et al. 2015). The multiple cores in BCGs at $z \lesssim 0.1$ also suggests a complex stellar mass growth of these objects over the past 4.5 Gyr (Hsu et al. 2022). This growth could be affecting the slope of the KR relation, but our results do not indicate this, either due to problems in determining their structural properties, or due to some mechanism regulating the growth in brightness and size of these galaxies. Differently, the slope variation for the HM ANC SAT is significant, which may be associated with both late accretion in the central region and the history of mergers in infall groups over the cluster evolution (e.g. Lopes et al. 2024). It is also important to mention that field galaxies do not present significantly different coefficients from the intermediate, recent and first infall samples, reinforcing the idea of evolution in ancient galaxies.

Therefore, our work is consistent with a scenario where giant ellipticals show a late growth, $z \lesssim 0.1$, either through infall group interactions or through interactions and accretion promoted by dynamic friction in the central region of the clusters. The combination of these evolutionary channels produce a significant effect on the

Kormendy relation, indicating that it can be used as an important indicator of the late evolution of cluster galaxies.

5 CONCLUSIONS

The study of ETGs is important to improve our understanding of the structure formation and the galaxy–environment connection. In this work, we investigated the KR of cluster ETGs according to their loci in the PPS. We have used a combination of statistical methods to identify possible differences between the fitted KR. From our analysis we can conclude that:

- The KR is better fitted when we take into account information about the PPS regions.
- There is a significant statistical difference between the KR coefficients of the ancient ETGs in relation to the others.
- The longer time within host clusters and the cumulative effect of mergers (in infall groups and/or in the central regions due to dynamical friction) plus accretion of stripped galaxies are the likely causes for the difference between the KR through the PPS regions. The relative importance of these mechanisms deserves a further study, to be presented in a forthcoming paper.
- HM ancient satellites are the component that most contributes to tilting the KR relation.
- A better determination of the brightness profile of BCGs and a larger sample of these objects can help to better understand the slope of the KR relation in the ancient region.

A possible caveat to this work is that we have not considered the effects of the velocity dispersion on the intrinsic scattering of the KR, a point to be examined in the future, in a complete study of the fundamental plane.

ACKNOWLEDGEMENTS

The authors thank the referee for useful suggestions. ALBR thanks the support of CNPq, grant 316317/2021-7 and FAPESB INFRA PIE 0013/2016. RSN thanks the financial support from CNPq, grant 301132/2020-8. PAAL thanks the support of CNPq, grants 433938/2018-8 e 312460/2021-0. CCD thanks the support by the Coordenação de Aperfeiçoamento de Pessoal de Nível Superior - Brasil (CAPES) - Finance Code 001, the Programa Institucional de Internacionalização (PrInt - CAPES), and the Brazilian Space Agency (AEB) for the funding (PO 20VB.0009). MHSF and FRMN thank the financial support by the Coordenação de Aperfeiçoamento de Pessoal de Nível Superior - Brasil (CAPES) - Finance Code 001. BGA thanks the support of PROBOL-UESC.

This research has made use of the SAO/NASA Astrophysics Data System, the NASA/IPAC Extragalactic Database (NED) and the ESA Sky tool (sky.esa.int/). Funding for the SDSS and SDSS-II was provided by the Alfred P. Sloan Foundation, the Participating Institutions, the National Science Foundation, the U.S. Department of Energy, the National Aeronautics and Space Administration, the Japanese Monbukagakusho, the Max Planck Society, and the Higher Education Funding Council for England.

DATA AVAILABILITY

The data that support the findings of this study are available on request from the corresponding author, A.L.B.R., upon reasonable request.

REFERENCES

- Aguado D. S., et al., 2019, *The Astrophysical Journal Supplement Series*, 240, 23
- Bender R., Burstein D., Faber S., 1992, *Astrophysical Journal*, Part 1 (ISSN 0004-637X), vol. 399, no. 2, p. 462-477., 399, 462
- Berlind A. A., et al., 2006, *ApJS*, 167, 1
- Biviano A., Murante G., Borgani S., Diaferio A., Dolag K., Girardi M., 2006, *A&A*, 456, 23
- Blanton M. R., Moustakas J., 2009, *Annual Review of Astronomy and Astrophysics*, 47, 159
- Chu A., Durret F., Márquez I., 2021, *Astronomy & Astrophysics*, 649, A42
- Conroy C., van Dokkum P. G., Kravtsov A., 2015, *The Astrophysical Journal*, 803, 77
- Djorgovski S., Davis M., 1987, *Astrophysical Journal*, 313, 59
- Domínguez Sánchez H., Huertas-Company M., Bernardi M., Tuccillo D., Fischer J. L., 2018, *MNRAS*, 476, 3661
- Dressler A., Shectman S. A., 1988, *The Astronomical Journal*, 95, 985
- Dressler A., Lynden-Bell D., Burstein D., Davies R. L., Faber S., Terlevich R., Wegner G., 1987, *Astrophysical Journal*, Part 1 (ISSN 0004-637X), vol. 313, Feb. 1, 1987, p. 42-58., 313, 42
- Fadda D., Girardi M., Giuricin G., Mardirossian F., Mezzetti M., 1996, *The Astrophysical Journal*, 473, 670
- Feldmann R., Carollo C. M., Mayer L., 2011, *The Astrophysical Journal*, 736, 88
- Genel S., et al., 2018, *Monthly Notices of the Royal Astronomical Society*, 474, 3976
- Gill S. P., Knebe A., Gibson B. K., 2005, *Monthly Notices of the Royal Astronomical Society*, 356, 1327
- Girardi M., Giuricin G., Mardirossian F., Mezzetti M., Boschin W., 1998, *ApJ*, 505, 74
- Gönen M., 2005, *Contemporary clinical trials*, 26, 131
- Goto T., 2005, *Monthly Notices of the Royal Astronomical Society*, 359, 1415
- Graham A., Colless M., 1997, *Monthly Notices of the Royal Astronomical Society*, 287, 221
- Hilz M., Naab T., Ostriker J. P., 2013, *Monthly Notices of the Royal Astronomical Society*, 429, 2924
- Hsu Y.-H., et al., 2022, *The Astrophysical Journal*, 933, 61
- Huang Y.-H., Chen H.-W., Johnson S. D., Weiner B. J., 2016, *Monthly Notices of the Royal Astronomical Society*, 455, 1713
- Inagaki T., Lin Y.-T., Huang H.-J., Hsieh B.-C., Sugiyama N., 2015, *Monthly Notices of the Royal Astronomical Society*, 446, 1107
- Jeffreys H., 1998, *The theory of probability*. OUP Oxford
- Johansson P. H., Naab T., Ostriker J. P., 2012, *The Astrophysical Journal*, 754, 115
- Kauffmann G., White S. D., Heckman T. M., Ménard B., Brinchmann J., Charlot S., Tremonti C., Brinkmann J., 2004, *Monthly Notices of the Royal Astronomical Society*, 353, 713
- Kelter R., 2022, *British Journal of Mathematical and Statistical Psychology*, 75, 550
- Kormendy J., 1977, *Astrophysical Journal*, Part 1, vol. 218, Dec. 1, 1977, p. 333-346. Research supported by the California Institute of Technology and National Research Council of Canada., 218, 333
- Kruschke J. K., 2018, *Advances in methods and practices in psychological science*, 1, 270
- Kruschke J. K., Liddell T. M., 2018, *Psychonomic bulletin & review*, 25, 155
- Kuchner U., Ziegler B., Verdugo M., Bamford S., Häußler B., 2017, *Astronomy & Astrophysics*, 604, A54
- Kuchner U., et al., 2022, *Monthly Notices of the Royal Astronomical Society*, 510, 581

La Barbera F., Busarello G., Merluzzi P., Massarotti M., Capaccioli M., 2003, *The Astrophysical Journal*, 595, 127

La Barbera F., Lopes P. A. A., de Carvalho R. R., de La Rosa I. G., Berlind A. A., 2010, *MNRAS*, 408, 1361

Laporte C. F., White S. D., Naab T., Gao L., 2013, *Monthly Notices of the Royal Astronomical Society*, 435, 901

Lock R. H., Lock P. F., Morgan K. L., Lock E. F., Lock D. F., 2020, *Statistics: Unlocking the power of data*. John Wiley & Sons

Longhetti M., et al., 2007, *Monthly Notices of the Royal Astronomical Society*, 374, 614

Lopes P. A. A., de Carvalho R. R., Kohl-Moreira J. L., Jones C., 2009, *MNRAS*, 392, 135

Lopes P. A., Ribeiro A. L., Brambila D., 2024, *Monthly Notices of the Royal Astronomical Society: Letters*, 527, L19

Makowski D., Ben-Shachar M. S., Lüdtke D., 2019, *Journal of Open Source Software*, 4, 1541

Mills J. A., 2018, *University of Cincinnati*

Morey R. D., Rouder J. N., 2011, *Psychological methods*, 16, 406

Naab T., Johansson P. H., Ostriker J. P., 2009, *The Astrophysical Journal Letters*, 699, L178

Neyman J., Pearson E. S., 1933, *Philosophical Transactions of the Royal Society of London. Series A, Containing Papers of a Mathematical or Physical Character*, 231, 289

Nigoche-Netro A., Ruelas-Mayorga A., Franco-Balderas A., 2008, *Astronomy & Astrophysics*, 491, 731

Nipoti C., Giocoli C., Despali G., 2018, *Monthly Notices of the Royal Astronomical Society*, 476, 705

Oser L., Ostriker J. P., Naab T., Johansson P. H., Burkert A., 2010, *The Astrophysical Journal*, 725, 2312

Peng Y.-j., et al., 2010, *The Astrophysical Journal*, 721, 193

Popesso P., Biviano A., Böhringer H., Romaniello M., Voges W., 2005, *A&A*, 433, 431

Popesso P., Biviano A., Böhringer H., Romaniello M., 2007, *A&A*, 464, 451

Ragone-Figueroa C., Granato G. L., Ferraro M. E., Murante G., Biffi V., Borgani S., Planelles S., Rasia E., 2018, *Monthly Notices of the Royal Astronomical Society*, 479, 1125

Reiprich T. H., Basu K., Ettori S., Israel H., Lovisari L., Molendi S., Pointecouteau E., Roncarelli M., 2013, *Space Science Reviews*, 177, 195

Rhee J., Smith R., Choi H., Yi S. K., Jaffé Y., Candlish G., Sánchez-Jánsen R., 2017, *ApJ*, 843, 128

Rhee J., Smith R., Choi H., Contini E., Jung S. L., Han S., Sukyoung K. Y., 2020, *The Astrophysical Journal Supplement Series*, 247, 45

Ribeiro A. L. B., de Carvalho R. R., Trevisan M., Capelato H. V., La Barbera F., Lopes P. A. A., Schilling A. C., 2013, *MNRAS*, 434, 784

Ribeiro A., Nascimento R., Morell D., Lopes P., Dantas C., Fonseca M., 2023, *Monthly Notices of the Royal Astronomical Society*, 521, 1221

Samir R., Takey A., Shaker A., 2020, *Astrophysics and Space Science*, 365, 142

Shen S., Mo H., White S. D., Blanton M. R., Kauffmann G., Voges W., Brinkmann J., Csabai I., 2003, *Monthly Notices of the Royal Astronomical Society*, 343, 978

Simard L., Mendel J. T., Patton D. R., Ellison S. L., McConnachie A. W., 2011, *The Astrophysical Journal Supplement Series*, 196, 11

Song H., Hwang H. S., Park C., Smith R., Einasto M., 2018, *The Astrophysical Journal*, 869, 124

Thomas D., Maraston C., Bender R., De Oliveira C. M., 2005, *The Astrophysical Journal*, 621, 673

Tortorelli L., et al., 2018, *Monthly Notices of the Royal Astronomical Society*, 477, 648

Trujillo I., Conselice C. J., Bundy K., Cooper M., Eisenhardt P., Ellis R. S., 2007, *Monthly Notices of the Royal Astronomical Society*, 382, 109

Van Dokkum P. G., et al., 2010, *The Astrophysical Journal*, 709, 1018

Yang X., Mo H., Van den Bosch F. C., Pasquali A., Li C., Barden M., 2007, *The Astrophysical Journal*, 671, 153

Ziegler B., Saglia R., Bender R., Belloni P., Greggio L., Seitz S., 1999, *Astron. Astrophys.*, 346, 13

de Carvalho R. R., Ribeiro A. L. B., Stalder D. H., Rosa R. R., Costa A. P., Moura T. C., 2017, *AJ*, 154, 96

van der Wel A., et al., 2014, *The Astrophysical Journal*, 788, 28

APPENDIX A: BAYESIAN HIPOTHESIS TESTING

A statistical hypothesis is a hypothesis about a particular model parameter or a set of model parameters. Bayesian approaches to hypotheses testing are foremost concerned, not with categorical decisions, but with quantifying evidence in favor or against the hypothesis in question. In this Appendix we briefly describe the methods used in Section 3.3. Here, in all cases the quantity to be tested is the difference of slopes and intercepts (δ) between two posterior distributions from the Bayesian regressions, with null hypothesis $\delta = 0$. The tests were done using functions contained in two R libraries: **bayesfactor** and **bayestestR**. In Figure A1 illustrates the most important elements of the Bayesian methods used in this work.

A1 Bayes Factor (BF) t-test

The Bayes factor is a wide used index for testing a hypothesis in the Bayesian approach (see e.g. Jeffreys 1998). To test the null hypothesis $\delta = 0$, a Cauchy prior with location zero and scale $r = 1/\sqrt{2}$ is used. For the variance σ^2 , Jeffreys's prior is used: $p(\sigma^2) \propto 1/\sigma^2$. In this example, we are interested in comparing the null model H_0 , which posits that the difference between the posteriors is zero, to the alternative hypothesis H_1 , which assigns δ the Cauchy prior. To compare the null model and the alternative model, we can compute the Bayes factor BF_{10} , that is, the Bayes factor which quantifies how much more likely the data are under the alternative versus the null hypothesis. BF_{10} is the Bayes factor giving evidence for H_1 over H_0 . The two-sample Bayesian t-test is done with the relationship between the hypotheses used in BF_{10} and the Student's t given by

$$H_0 : t \sim T_\nu, \quad \text{and} \quad (A1)$$

$$H_1 : \frac{t}{\sqrt{1 + \sigma_\delta^2 N}} \sim T_\nu \left(\frac{\delta}{\sqrt{1/N + \sigma_\delta^2}} \right) \quad (A2)$$

where T_ν represents the standard (central) T distribution with ν degrees of freedom, and $T_\nu(\theta)$ is the non-central T distribution with argument θ (e.g. Gönen 2005).

A2 Maximum A Posteriori (MAP)

The MAX-based p-value is defined as the ratio of the posterior densities null value $p(\theta_0)$ and the posterior densities maximum a posteriori (MAP) value:

$$p_{\text{MAP}} = \frac{p(\theta_0|x)}{\arg \max_{\theta \in \Theta} p(\theta|x)} \quad (A3)$$

where $\theta_0 = \delta = 0$. The test is based on the likelihood ratio used in the Neyman-Pearson theory (Neyman & Pearson 1933). The denominator is not maximising the likelihood over the alternative hypothesis H_1 like in a traditional Neyman-Pearson test, but instead the posterior density $p(\theta|x)$ is maximised. The MAP-based p-value is the ratio between the posterior distribution's value at the null value $\theta = 0$ and the maximum of the distribution (Mills 2018).

A3 Region of Practical Equivalence (ROPE)

The general idea of this test is to establish a region of practical equivalence around the null value θ_0 of the null hypothesis $H_0 : \theta = \theta_0$, which express the range of parameter values that are equivalent to the null value for practical purposes (Kruschke & Liddell 2018). To test hypotheses via the ROPE we need to find the highest posterior density (HPD) interval, which is basically the shortest interval on a posterior density for some given confidence level. Kruschke (2018) proposed the following decision rule:

- Reject the null value θ_0 specified by $H_0 : \theta = \theta_0$ ($\delta = 0$), if the 95% HPD falls entirely outside the ROPE.
- Accept the null value, if the 95% HPD falls entirely inside the ROPE.

Hence, if the 95% HPD falls entirely inside the ROPE, the parameter value is located inside the ROPE with at least 95% posterior probability. As a consequence, it is practically equivalent to the null value θ_0 and it is reasonable to accept H_0 (see Makowski et al. 2019).

A4 Probability of Direction (PD)

The probability of direction (PD) is defined as the proportion of the posterior distribution that is of the median's sign, is a measure of effect existence representing the certainty with which an effect is positive or negative. Therefore, the PD is simply the proportion of the posterior probability density which is of the median's sign. Based on the PD, one can test the null hypothesis $H_0 : \delta = 0$ by requiring a specified amount of posterior probability density to be strictly positive or negative. Usually, more than 95% of the posterior can be used as threshold for deciding between H_0 and H_1 . The two-side p-value is obtained as

$$p_{PD} = 2 \cdot (1 - PD). \quad (A4)$$

(see Makowski et al. 2019).

This paper has been typeset from a \LaTeX file prepared by the author.

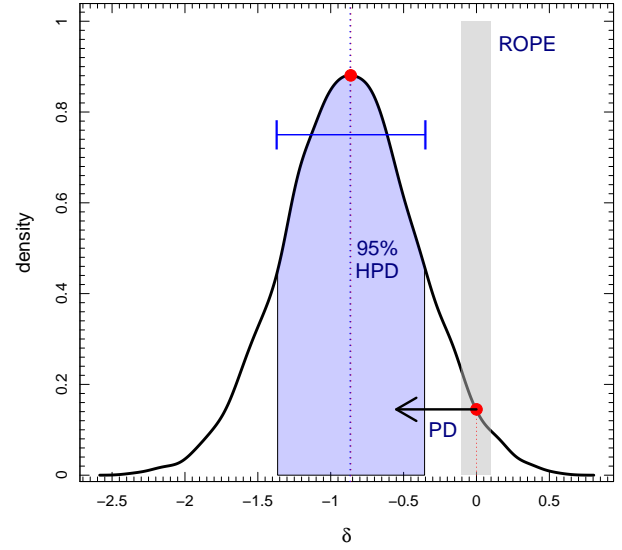


Figure A1. Figure illustrating the most important aspects of the Bayesian methods used in this work. The gray shade area shows the ROPE, while the blue shaded area corresponds to the posterior probability inside the 95% HPD. For the likelihood ratio, points in red are showed, and for the computation of the PD area, the arrow indicates the lower limit of the density distribution integral, which extends to $-\infty$.